Article

Dry Cold Forging of High Strength AISI316 Wires by Massively Nitrogen Supersaturated CoCrMo Dies

Tatsuhiko Aizawa [1,*] **, Tatsuya Fukuda** [2] **and Tomomi Shiratori** [3]

[1] Surface Engineering Design Laboratory, Shibaura Institute of Technology, Tokyo 144-0056, Japan
[2] Tokai Engineering Service, Co., Ltd., Kyoto 601-8306, Japan; t-fukuda@tes2001.com
[3] Faculty of Engineering, University of Toyama, Toyama 930-8555, Japan; shira@eng.u-toyama.ac.jp
[*] Correspondence: taizawa@sic.shibaura-it.ac.jp; Tel.: +81-3-6424-8615

Abstract: The plasma immersion nitriding system was utilized to make massive nitrogen supersaturation (MNS) to CoCrMo disc and die substrates at 723 K for 21.6 ks. The top layer thickness in the multi-layered MNSed layer was 20 μm. Its nitrogen solute content reached 5 mass% on average after SEM-EDX analysis. The surface hardness was 1300 HV_{1N} ($HV_{0.1}$), which was much higher than the bare CoCrMo with 450 HV_{1N}. The original polycrystalline structure was modified to be a multi-layered microstructure, which consisted of the nanograined MNSed top layer, the buffer layer with a thickness of 5 μm, and the column–granular structured layer with their textured crystallographic orientations. The BOD (ball-on-disc) testing was employed to describe the frictional sliding behavior under the applied loads of 5 N and 10 N and the sliding velocity of 0.1 m/s against the AISI316 ball. The friction coefficient was held constant by 0.68 on average. The CNC (Computer Numerical Control) stamping system was employed to upset the fine-grained 1.0 mm thick AISI316 wire up to 70% in reduction in thickness. The friction coefficient at RT was estimated to be 0.05. A round, fine-grained AISI316 wire was shaped into a thin plate with a thickness of 0.3 mm in cold and dry.

Keywords: CoCrMo; superalloy dies; dry; cold forging; massively nitrogen supersaturation; high surface hardness; intensely textured microstructure; fine-grained AISI316; medical applications

1. Introduction

Fine-grained AISI316 wires and beams have been highlighted as a structural member of medical tools and equipment because of their high strength and mechanical performance without loss of ductility and toughness [1]. However, their high strength and high surface hardness hindered the engineering way to form them into complex-shaped parts. Mechanical machining is only a means to build up those parts [2]. A metal forming and near-net forging of these high-strength AISI316 with advanced die technology is expected as an innovative solution for manufacturing medical tools and parts in mass production.

Ni-base and Co-base superalloys have been utilized in various applications where high wear resistance and long part-life were required in practice [3]. A bulk CoCrMo superalloy was utilized for hip replacement and dental prosthesis [4,5]. It was further used as a hot-extrusion die to fabricate the aluminum alloy rods with low adhesive wear [6]. As stated in [7], the bare CoCrMo only has a surface hardness of 400 to 450 HV, much lower than the strength of fine-grained AISI316 work. Various surface treatments were developed to improve the mechanical properties of these bare CoCrMo alloys in the literature [8]. Among them, nitriding processes were developed to further improve the strength and hardness of original CoCrMo superalloys [9,10]. In particular, the surface hardness was improved up to 1000 HV even using the HIPIMS (High Power Impulse Magnetron Sputtering) [11]. This high hardness was expected to provide a solution for mold-stamping dies of oxide glass lenses and optical elements above their glass transition temperature [12].

For further advancement of the cold and hot forging of difficult-to-form work materials using CoCrMo supper alloy dies, their microstructural control must be indispensable

from the top layer to the bare CoCrMo matrix. As depicted in Figure 1, a multi-layered material system is preferable to forging dies [13]. The top layer has a nanostructured system with high strength and hardness due to grain size refinement [14]. The externally applied stress to this top layer is transferred to the depth of the die through the buffer layer and supported by the columnar structure, each longitudinal grain of which has a textured crystallographic orientation. In particular, these textured columnar grains have heat resistance even in hot forging in a similar manner to nickel-base single crystals [15] or intermetallic compounds [16]. The massive nitrogen supersaturation (MNS) was developed to impinge the nitrogen interstitial solutes into the superalloys and to store them in high concentration [7,17,18]. This MNSed layer, synthesized at 673 K, had a unique microstructure. It was composed of the nanostructure top layer with a thickness of 10 μm and an intense texture to (111), and the buffer zone with a thickness of 2 μm onto the CoCrMo matrix. Higher hardness than 1500 HV_{1N} and lower friction with μ < 0.5 mechanically characterized this multi-layered system synthesized at 673 K. This formation of the multi-layered structure was significantly controlled by the plasma nitriding immersion conditions, such as the holding temperature and total gas pressure.
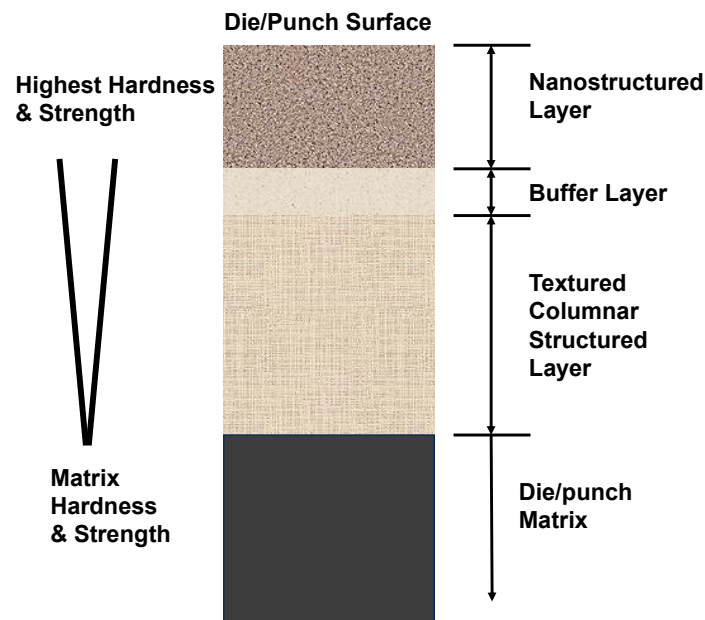

Figure 1. A schematic view of the surface-engineered die to have a multi-layered system by massive nitrogen supersaturation into a standard polycrystalline die material.

In the present study, this MNS process is performed by the plasma immersion nitriding process at 723 K to modify the bare microstructure of the CoCrMo super alloy die and to build the multi-layered die-material system into the CoCrMo matrix after Figure 1. The BOD (ball-on-disc) testing is employed to describe the frictional sliding behavior under the applied loads of 5 N and 10 N and the sliding velocity of 0.1 m/s. AISI316 ball is used as a counter material. The friction coefficient (μ) is held constant by 0.68 on average, irrespective of the applied load. The CNC (Computer Numerical Control) stamping system is employed to upset the fine-grained AISI316 bar with a diameter of 1.0 mm and a length of 10 mm to the specified reduction in thickness (r). Owing to relatively low friction on the contact surface of massive nitrogen supersaturated (MNSed) CoCrMo dies to AISI316 work, the initial round bar is upset to a plate with a little bulging deformation.

2. Materials and Methods

The plasma immersion nitriding system was stated for the massive nitrogen supersaturation process. The upsetting system was also explained for the experimental setup. The die and work materials were defined by their chemical compositions.

2.1. Massive Nitrogen Supersaturation

The plasma immersion nitriding system (NS-1; YS-Electrical Industry, Co., Ltd.; Kofu, Japan) was utilized to make MNS treatment of CoCrMo substrates and dies at 723 K for 21.6 ks. The plasma nitriding unit is illustrated in Figure 2a. RF (Radio Frequency) and DC (Direct Current) generators were used to ignite the nitrogen–hydrogen plasmas at the specified temperature and pressure. Through the optically flat silica window, the plasma state was monitored for plasma diagnosis. The hollow cathode device was employed to densify the nitrogen ion and NH radical populations, as reported in [19,20]. The thermal transient was also monitored by using the thermocouple, which was embedded into the substrate below the hollow. As shown in Figure 2b, this plasma nitriding system consisted of the vacuum chamber, the automatic gas supply, the evacuation unit, and the control panel. The temporal mismatch between input and output powers was self-adjusted by tuning the frequency around 2.08 MHz.
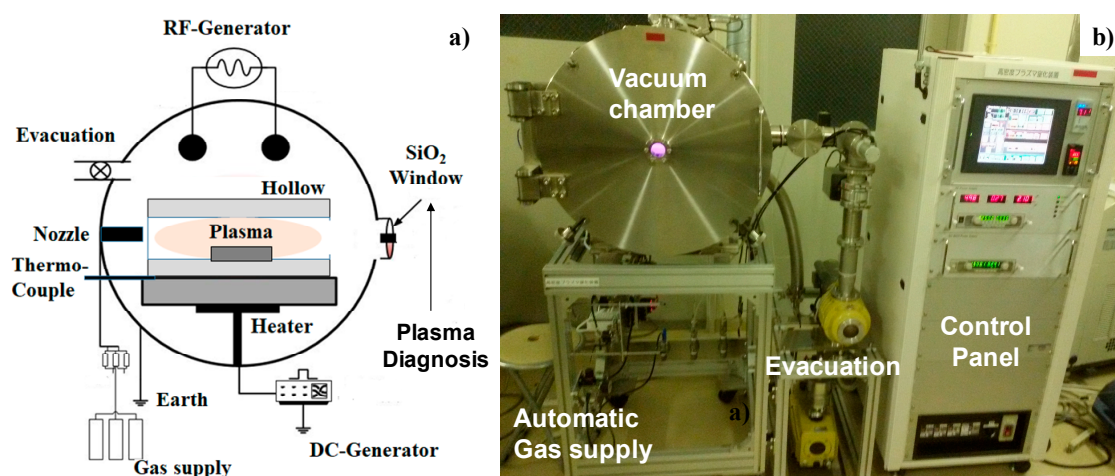

Figure 2. Nitrogen plasma immersion system for nitrogen supersaturation process. (**a**) Its schematic view, and (**b**) its overview.

In the MNS process, the CoCrMo disc specimen and dies were fixed into the hollow cathode before evacuation to the base pressure of 0.1 Pa. After heating up to 723 K in the nitrogen atmosphere, the hydrogen gas was introduced for pre-sputtering only by using the DC bias of -500 V. The pure nitrogen and hydrogen gases, with a purity of 99.99%, were utilized as sources. Their flow rates were 160 mL/min and 30 mL/min, respectively. In particular, the hydrogen gas supply is indispensable to synthesizing NH radicals in nearly the same population as N_2^+, mother nuclei to synthesize {N^*, N^+, and N^{2+}} in a series of reactions in the plasmas. After pre-sputtering at 723 K by 60 Pa for 1.8 ks, the MNS process was performed at 723 K by 60 Pa for 21.6 ks after reference to experimental results in [7]. Both RF and DC plasmas were utilized under the RF voltage of +250 V and the DC bias of -500 V. After nitriding, the experimental setup was cooled down to RT under the nitrogen atmosphere. In the plasma diagnosis, highly bright optical emission from the hollow in Figure 3 proves that the densification of nitrogen ion and NH radical populations in the plasma immersion is indispensable for MNS to obtain the sufficient thickness of the MNSed layer and to improve the surface hardness.
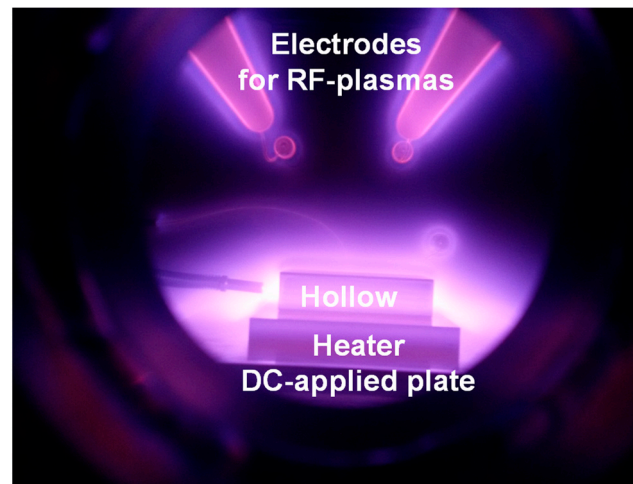
Figure 3. Nitrogen–hydrogen plasma sheath surrounding the CoCrMo die at 723 K.

2.2. Upsetting Process

An MNSed CoCrMo cylindrical substrate pair was, respectively, utilized as the upper and lower dies in the upsetting process. These dies were, respectively, locked into the upper and lower die sets for upsetting experiments to the specified reduction in thickness (r) in a single stroke. The experimental setup is depicted in Figure 4. The stroke was directly controlled in this CNC (Computer Numerical Control) stamping. The applied load was monitored by the load cell embedded into the lower die. The stroke velocity was constant by 10 mm/s.
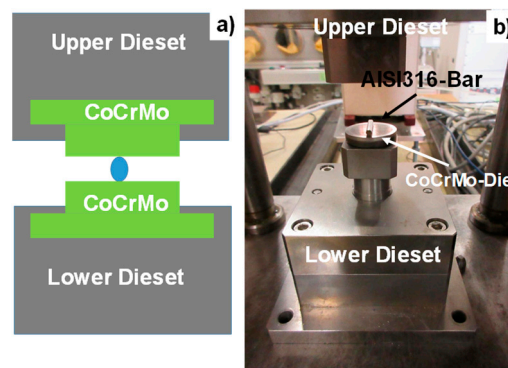

Figure 4. Upsetting experimental system. (**a**) A schematic view of the upsetting experimental unit, and (**b**) an overview of the upsetting system.

CoCrMo cylindrical dies were fabricated by cutting and polishing the raw feedstock. Its chemical compositions are listed in Table 1. AISI316 bar, with the refined grain size down to the specified diameter by intense rolling [21], was utilized as a work material in forging. Its diameter and length were 1.0 mm and 10.0 mm, respectively. The SEM image on the bare CoCrMo die is shown in Figure 5. Its microstructure was characterized by an equi-axial granular structure with an average grain size of 30 μm.

Table 1. Chemical compositions of CoCrMo die materials.

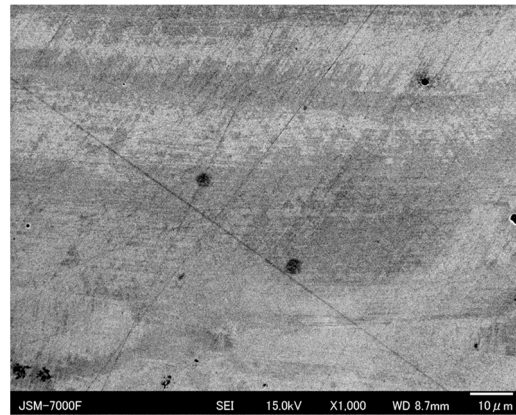| Element	Cr	Mo	Si	Mn	Fe	Ni	N	C	Co
Content	27.14	5.99	0.59	0.61	0.06	<0.01	0.11	0.052	Balance

mass%.

Figure 5. SEM image on the cross-section of bare CoCrMo die materials before plasma nitriding immersion.

2.3. Microstructure and Mechanical Characterization

The MNSed CoCrMo specimen is characterized by XRD (X-ray diffraction), SEM (Scanning Electron Microscopy), and EDX (Electron Dispersive X-ray spectroscopy). SEM (JEOL, Tokyo, Japan) and EDX (JEOL, Tokyo, Japan) were employed to analyze the SEM image and nitrogen solute mapping on the cross-section of the MNSed CoCrMo die. EBSD (Electron Back-Scattering Diffraction; JEOL, Tokyo, Japan) was utilized to analyze the cross-sectional microstructure of the MNSed layer. It is also mechanically characterized by micro-hardness testing and the ball-on-disc method. The tribotesting system Rigaku SmartLab, Version-7 (CSM; Bern, Switzerland) was utilized to make ball-on-disc testing and to describe the frictional behavior of the MNSed CoCrMo die against the AISI316 ball with a diameter of 6 mm. The AISI316 bar is upset at the specified reduction in thickness by MNS-CoCrMo dies.

3. Results

3.1. Massive Nitrogen Supersaturation to CoCrMo Dies

MNSed CoCrMo at 723 K for 21.6 ks was analyzed by XRD (Rigaku SmartLab, CSM, Co., Ltd., Bern, Switzerland) with monochromatic CuKα radiation (λ = 0.1542 nm) and Bragg–Brentano geometry, 40 kV, and 30 mA. The 2θ range was set between $36°$ and $55°$ with a scanning speed of 1.0 s/step and a step angle of $0.01°$. XRD diagram before MNS was characterized by two γ-peaks at $2\theta = 43.67°$ and $2\theta = 50.75°$, respectively. As reported in [17,18], these two peaks shifted themselves by MNS at 673 K for 14.4 ks to $2\theta = 40.28°$ and $2\theta = 46.04°$, respectively. That is, the γ-lattices of CoCrMo grains expanded by MNS at 673 K as detected by γ_N phase peaks in the XRD diagram. On the other hand, as seen in Figure 6, two γ_N peaks were detected at $2\theta = 43.95°$ and $2\theta = 50.80°$. No peak shift was induced by MNS at 723 K.
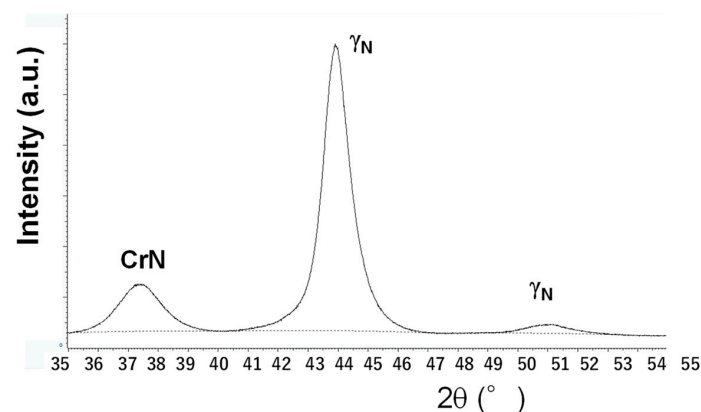

Figure 6. Comparison of XRD diagram for CoCrMo die after MNS at 723 K for 21.6 ks.

This insensitivity of peak shift to MNS might come from CrN precipitation. A broad peak of CrN was detected at 2θ = 37.55°; after [22], fine CrN precipitates are formed to compress the grain expansion due to their pinning effect. This suppression of lattice expansion by fine CrN precipitates cancels the lattice expansion by MNS in the vicinity of the surface. Figure 7 shows the cross-sectional SEM image and nitrogen mapping, respectively. Nitrogen is detected homogeneously on the surface and on the cross-section. At point P_1 on the cross-section in Figure 7a, the nitrogen content is more than 5 mass%.
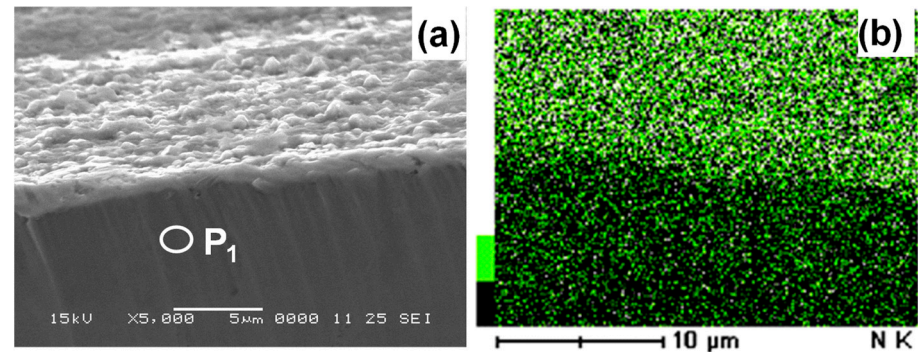

Figure 7. SEM image and nitrogen map on the cross-section of MNS-CoCrMo dies. (**a**) SEM image on the cross-section of MNSed CoCrMo, and (**b**) nitrogen mapping.

In a similar manner to this pointwise nitrogen content analysis at P1 in Figure 7a, the nitrogen content depth profile was analyzed down to the depth of 120 µm. As depicted in Figure 8, a higher nitrogen content than 15% was detected in the vicinity of the MNSed surface layer in Figure 7b. This nitrogen content decreased exponentially across the MNSed layer thickness down to 4 at% at the depth (d) of 35 µm. To be noticed, the nitrogen content was preserved to be 2 to 4 at% for d > 40 µm down to 120 µm.
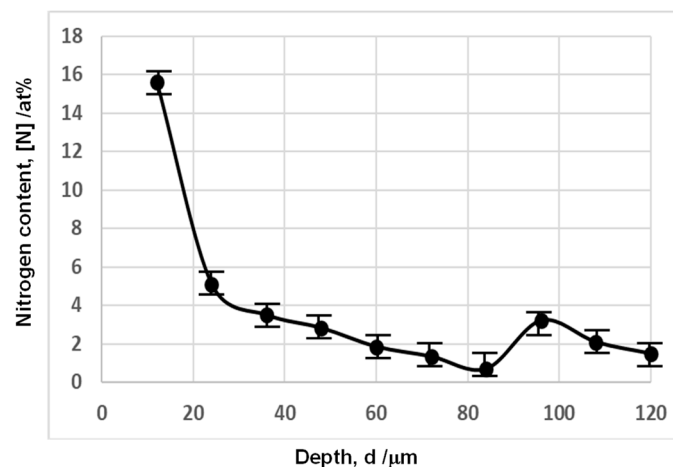

Figure 8. Variation of the nitrogen solute content pointwise analyzed by EDX from the surface down to the depth of 120 µm.

After [23], the Kikuchi pattern or its IQ (Image Quality) is sensitive to crystallographic defects such as the grain boundaries and the plastic strains in the slip-line field. The nanograins and the slip-line fields are represented by the black-out and the black lines, respectively, in EBSD analysis [23]. The inverse pole figure (IPF) represents the crystallographic orientation of each grain. The KAM (Kernel angle misorientation) corresponds to the plastic strains; the plastically induced slip-lines are represented by the crossing lines with higher KAM in this KAM map.

After low magnification EBSD in Figure 9, the equi-axial granular structure of bare CoCrMo in Figure 4 was modified to have a multi-layered structure, which is composed of

the nanostructured top layer with the thickness of 20 µm, the buffer layer in 5 µm thickness, and the column–granular structure till the depth of 700 µm. This top layer is, respectively, characterized by the black-out in the IQ map, by the multi-colored region in the IPF map, and by the white-out in the KAM map. The original granular microstructure is modified to have a nanostructured top layer by grain size refinement via plastic straining in high intensity. This highly plastic straining is induced just below the nitriding front end in neighboring to nitrided zones with lattice expansion in order that the strain compatibility is preserved across the frond. The slip-line fields in Figures 9 and 10 with high KAM are formed in the cross-section of the MNSed microstructure. The buffer layer has the transient microstructure between the top layer and the column–granular structure. Each grain in the column–granular layer has slip-line fields and graded crystallographic orientations, as proved by their IQ, KAM, and IPF maps. High KAM zones correspond to black lines in the IQ map and the grading pattern in the IPF map, respectively. The crystallographic orientations and subgrain refinement must be driven by intense plastic straining through these longitudinal grains.
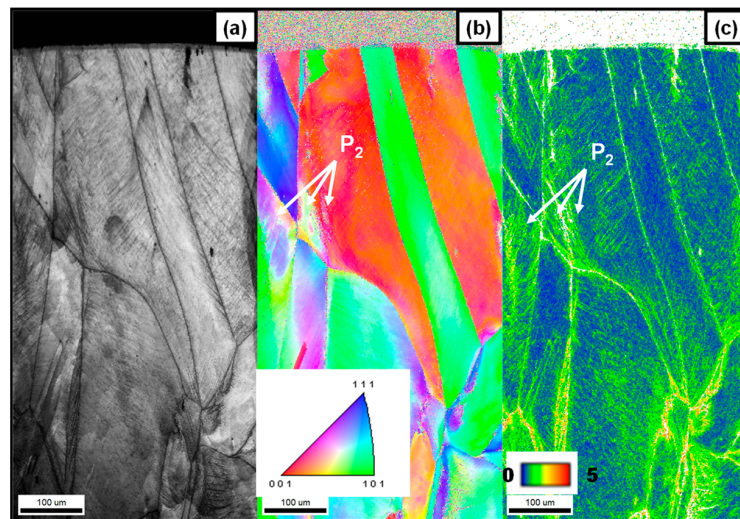

Figure 9. EBSD analysis on the cross-section of MNS-CoCrMo dies under low magnification. (**a**) IQ map, (**b**) inverse pole figure, and (**c**) kernel angle misorientation (KAM) map.
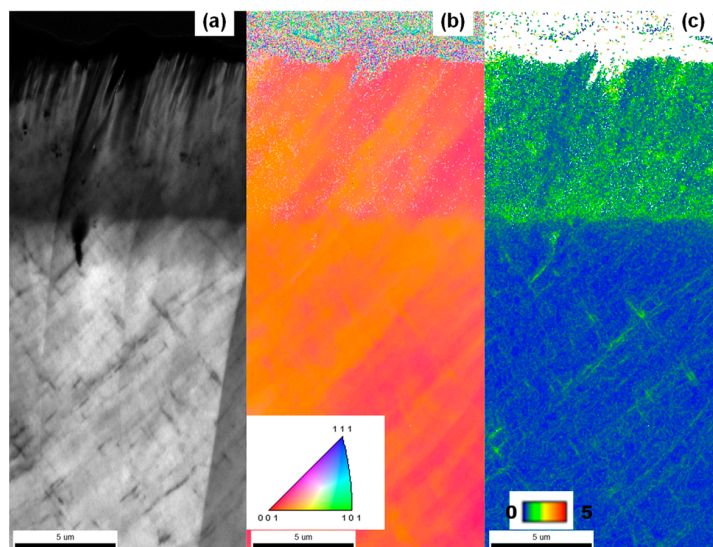

Figure 10. High magnification EBSD analysis on the cross-section of MNS-CoCrMo dies from the top layer to the textured layer across the buffer zone. (**a**) IQ map, (**b**) IPF map, and (**c**) KAM distribution.

High magnification EBSD was utilized to analyze the modification of granular structure from the top layer to the textured depth across the buffer layer. As shown in Figure 10, the nano-granular structure in the top layer changes by themselves across the buffer layer to the graded granular structure in the column-structured layer. After the IQ map, in parallel with this nanostructure change, the black-out in the top layer changes to the slip-line fields through the grayed buffer zone. The high intensity of KAM also changes the cross-lined KAM distributions in the graded granular structure through the buffer layer with lower KAM. That is, the plastic straining across the buffer layer propels the nano-structuring of bare CoCrMo during the MNS process. Considering that nitrogen content decays exponentially through the buffer layer in Figure 8, this buffer layer represents the front end of the MNS process to drive the nanostructuring and intense plastic straining in homogeneous and synthesize the nanostructured and highly strained top layer. Below this front end, this nanostructuring and plastic straining advances in local and heterogeneous. Although the average nitrogen content is only 2 to 4 at% in Figure 8, a local nitrogen solute concentration is much more than this average enough to drive the MNS process locally and heterogeneously. In fact, the nanograins and high KAM regions are detected at d = 400 μm, respectively, in Figure 9b,c, as pointed by white arrows at P_2.

3.2. Mechanical Characterization

Hardness measurement was first employed to describe the hardness depth profile on the cross-section of the MNSed CoCrMo die. The top layer was mechanically ground and polished to the specified depth for measurement of hardness. Figure 11 depicts the measured hardness depth profile. The hardness is nearly constant by 1300 HV_{1N} ($HV_{0.1}$) down to 30 μm in-depth, equivalent to the surface hardness. This reveals that both the nanostructured top layer and transient buffer layer have sufficiently high hardness due to MNS treatment. The nanogranular structure of MNSed CoCrMo is responsible for this hardening behavior.
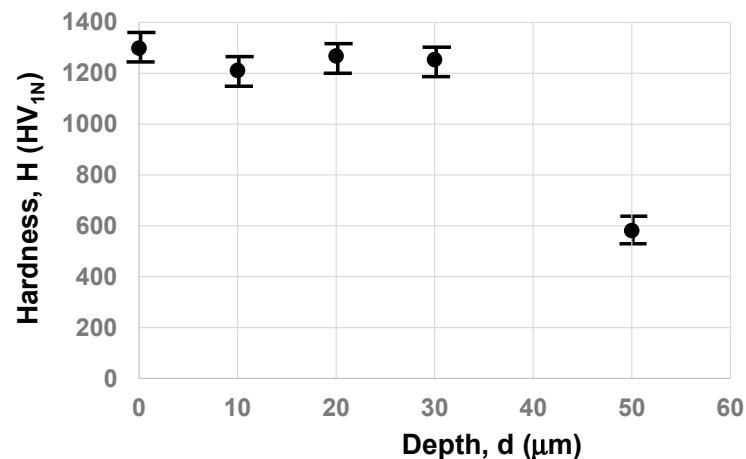

Figure 11. Hardness depth profile on the cross-section of MNSed CoCrMo from the surface to the depth.

Below the buffer layer, this hardness gradually decreases with d down to 600 HV1N on average. After Figures 9 and 10, the MNS process advances to the depth homogeneously and uniformly synthesizes the nanograined layer to d = 20–25 μm. Below the buffer layer, this homogeneous MNS process turns to heterogeneous so that nitrogen solutes diffuse only through the slip-line field in the grains and that the plastic straining by MNS takes place locally in this textured layer. Hence, this heterogeneous MNS reflects on the hardness in depth; the locally MNSed zones have higher hardness, but less MNSed zones have lower hardness. The hardness distribution from the surface to the depth of 1.0 mm with a spatial resolution of 50 μm. Figure 12 depicts the hardness mapping from the vicinity of the surface to the depth at d = 1.0 mm. As predicted, higher hardness than 500 HV is measured just

below the buffer layer to the depth of 200 μm; lower and higher hardness regions are seen alternatively in depth. The column–granular structure in Figures 9 and 10 is mechanically characterized by this heterogeneous hardness map.
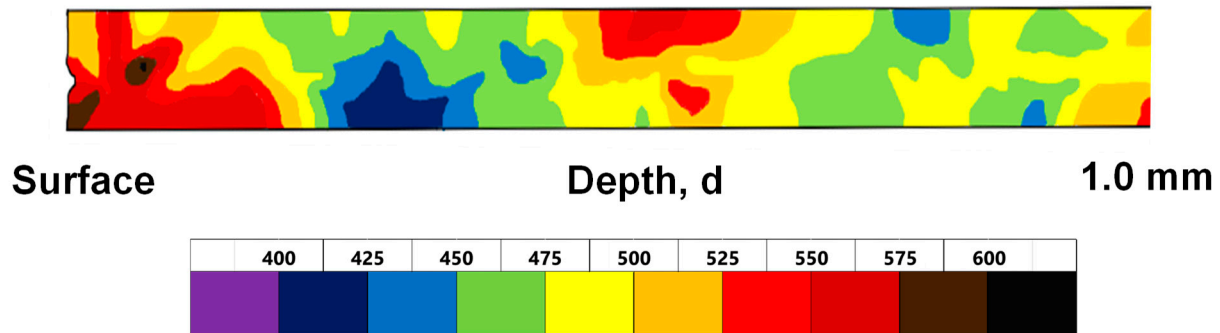

Figure 12. Hardness mapping from the vicinity to surface to the depth at d = 1.0 mm. The textured layer in Figures 9 and 10 down to d = 120 μm has higher hardness than 550 HV.

The applied load (W) was varied to be 5 N and 10 N. The sliding velocity was constant by 0.1 m/s. As depicted in Figure 13, when W = 5 N, the measured friction coefficient (μ) is preserved to be μ~0.65 with a deviation (Dμ) of 0.03. This frictional transient with increasing the siding distance was insensitive to the applied load as shown in Figure 14. When W = 10 N, μ~0.65 and Dμ = 0.04 till L = 100 m become the same transient of μ and Dμ for W = 5 N in Figure 13.
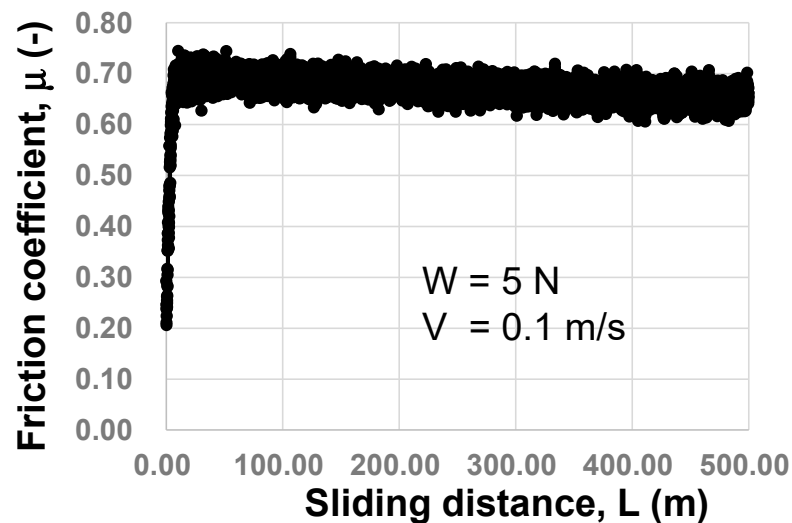

Figure 13. Variation of the friction coefficient for the MNS-CoCrMo disc against the hard AISI316 ball under W = 5 N and V = 0.1 m/s till the sliding distance of 500 m.

As stated in [24], the adhesive wear is generally enhanced by increasing the applied load since the fresh surface of work materials is sticking to their adherent debris onto dies. No significant change in the measured frictional transients in Figures 13 and 14 proves that little galling takes place on the contact surface of the MNSed CoCrMo disc to the AISI316 counter material. That is, the AISI316 ball is worn out in itself by its plastic deformation and flow against the MNSed CoCrMo substrate.
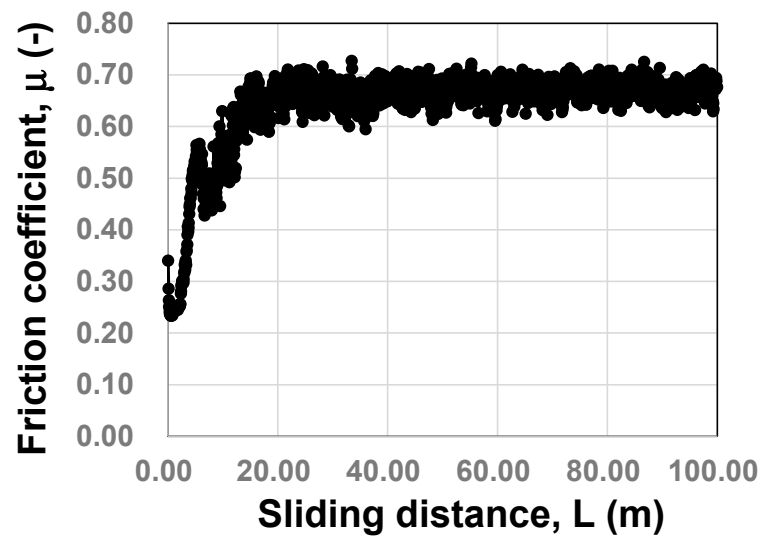
Figure 14. Variation in the friction coefficient for the MNS-CoCrMo disc against the hard AISI316 ball under W = 10 N and V = 0.1 m/s till the sliding distance of 100 m.

The worn-out AISI316 ball surface after BOD testing till L = 500 m under W = 5 N and V = 0.1 m/s was analyzed by optical microscopy, as shown in Figure 15. The metal flow trace of AISI316 was seen on the worn-out surface. The AISI316 ball was abrasively worn out without adhesion of work material to the MNSed disc. This also proves that little galling takes place on the contact surface of the MNSed CoCrMo disc to the AISI316 ball.
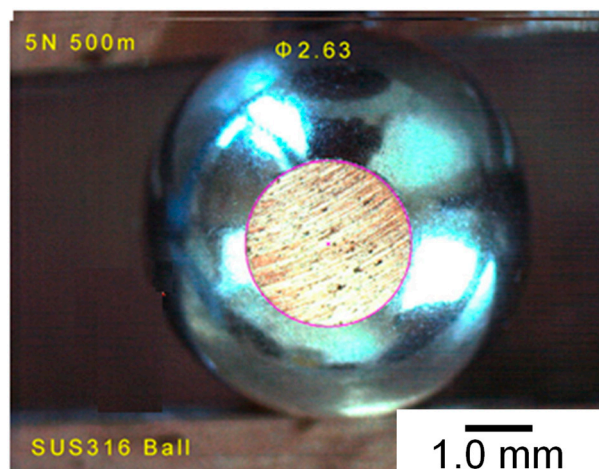

Figure 15. Analysis of the worn-out volume of the AISI316 ball against the MNSed CoCrMo disc after BOD texting till L = 500 m under W = 5 N and V = 0.1 m/s.

3.3. Upsetting Behavior of Fine-Grained AISI316 Work Materials

A fine-grained AISI316 bar for medical and tooling applications was utilized as a work for upsetting with the use of MNSed CoCrMo dies. When using the bare CoCrMo dies with an average hardness of 450 HV_{1N}, the AISI316 work caved into the CoCrMo die to leave the concave trace into the die. This is because the fine-grained AISI316 work has higher strength and hardness than that of the bare CoCrMo hardness.

Figure 16 depicts the variation of upset AISI316 wire with increasing the reduction in thickness (r) up to 70% by using the MNSed CoCrMo dies. No traces of adhesives and damages were seen on the MNSed CoCrMo die surface. This reveals that the MNSed CoCrMo die has sufficient surface hardness against the highly strengthened AISI316 by intense rolling [21]. In particular, no shear localization during upsetting [25] was seen even in the trace level on the cross-section of the upset fine-grained AISI316 bar, even at r = 70%.

The AISI316 work homogeneously flattens with increasing r. This suggests that the friction coefficient on the work-die interface is relatively low and that the workflow velocity in the vicinity of the die surface is nearly the same as that at the center of the work. After [26], the bulging deformation B_g, which is defined by $Bg = (W_o - W_i)/2$, is employed as a parameter to measure the frictional behavior for the measured work width (W_o) and interface width (W_i), respectively. As depicted in Figure 17, ($W_o - W_i$) or B_g monotonously decreases and goes to nearly zero with increasing r. This proves that AISI316 work plastically deforms and flattens in relatively low friction. After the empirical relationship between B_g and μ in [26], μ is estimated to be 0.05 from Figure 17.
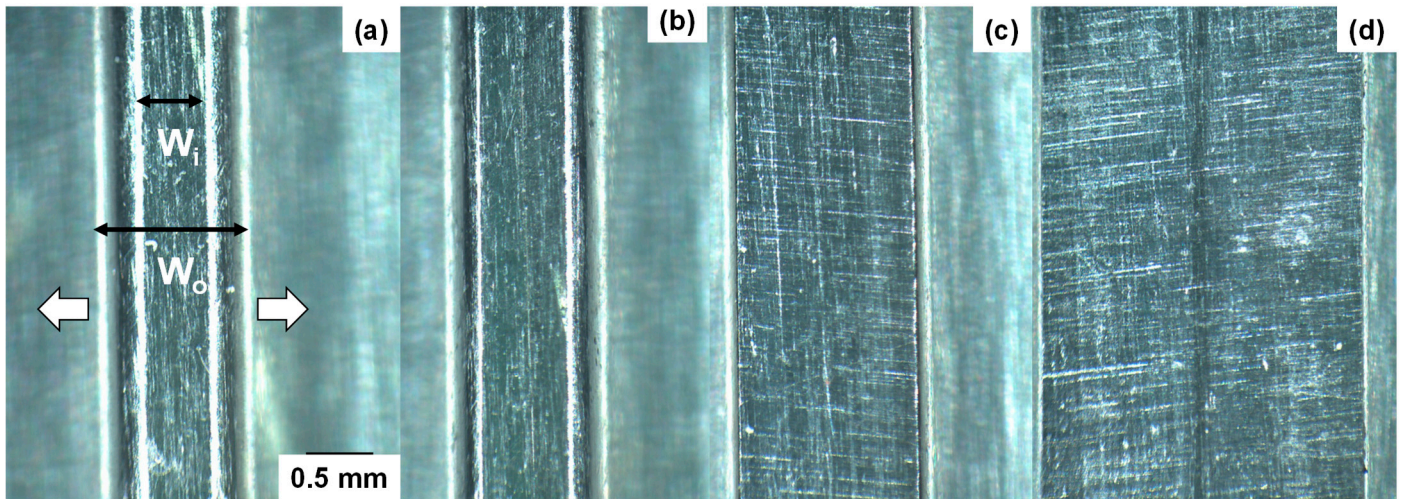

Figure 16. Variation in the cross-section view for the forged AISI316 works with increasing the reduction in thickness. (**a**) r = 10%, (**b**) r = 20%, (**c**) r = 50%, and (**d**) r = 70%. White arrows indicate the direction of plastic deformation.
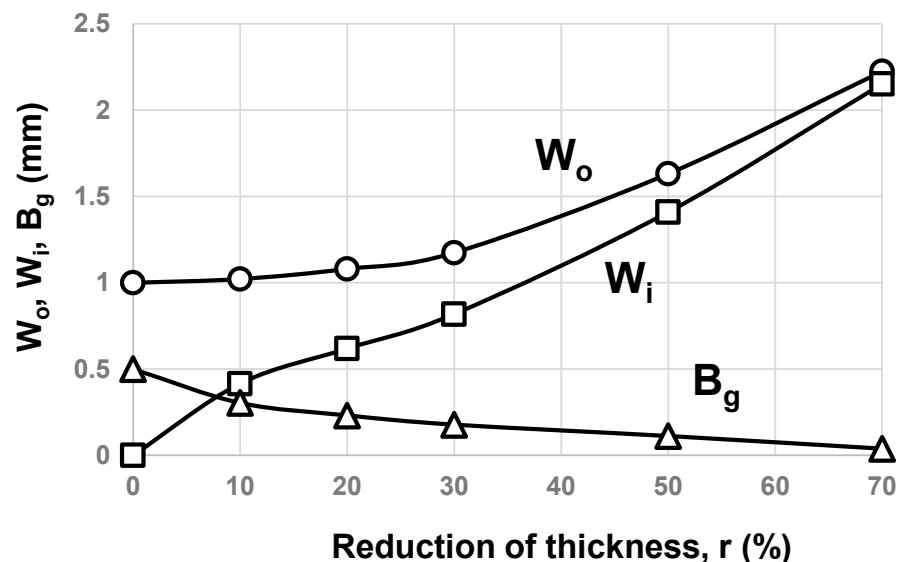
Figure 17. Variation in the bar width (W_o), the contact interface width (W_i), and the nondimensional bulging displacement (B_g) with increasing r.

4. Discussion

Massive nitrogen supersaturation (MNS) works to modify the homogeneous, equi-axial crystallographic structure of superalloy to a multi-layered structure. The top layer is nanograined CoCrMo with a random crystallographic orientation. The buffer layer has partially nanograined CoCrMo but a mixture with the textured grains growing in the

specific crystallographic orientations. In the column-structured layer below the buffer layer, an assembly of CoCrMo subgrains forms long and large grains onto the original CoCrMo matrix. The MNS process is characterized by this systematic surface modification. After the theoretical study on the nitriding of α-iron [27] and the experimental study on the plasma nitriding of various stainless steels [28], the neighboring regions to the nitrided zones with lattice expansion are plastically strained to compensate for the strain compatibility across the nitriding front end. The in situ formed slip-lines and nanograin boundaries by plastic straining become a nitrogen solute diffusion path network to further advance the MNS process into depth.

As depicted in Figures 9 and 10, the buffer layer plays the role of nitriding the front end, where the homogeneous MSE process changes to the heterogeneous MSE process due to the exponential decay of nitrogen solute content. The homogeneous MSE process is accompanied by a crystallographic modification to nanograins. High nitrogen solute content is preserved by an active nitrogen solute diffusion through the nanograin boundaries and the slip-line fields induced by the plastic straining. The heterogeneous MSE process advances with local plastic straining to form the slip-line fields in each grain and spin rotation to modify the original crystallographic orientation in each grain. This difference in the MSE process influences the hardness depth profile in Figure 11. High hardness is uniformly attained by homogeneous MSE above the buffer layer, while hardness gradually decreases below the buffer layer by heterogeneous MSE.

A hardness profile design in the die technology is essential to prolong the die life and to control the process tribology [29]. Most of those studies stand on the hard coating onto the die surface [30] and on the duplex approach, where various ceramic hard coating layers are deposited onto the nitrided dies [31]. In the present approach, the top and buffer layers with higher hardness than 1300 HV_{1N} are formed on the textured granular CoCrMo layer with its gradual hardness grating from 600 HV_{1N} to the hardness of bare CoCrMo by 450 HV_{1N} without the use of any coatings. Different from conventional thin and hard coatings, a thick MNS-later with higher hardness than 1300 HV_{1N} protects the die and mold from abrasive wear during cold and hot stamping. The success of hot aluminum extrusion by CoCrMo in [4] suggests that the MNSed CoCrMo diet plays a role in significantly reducing the adhesive wear in practice. This hardness grading system by the multi-layered microstructure is preferable to a die and mold substrate.

A fine-grained AISI316 wire with a diameter of 1.0 mm is upset and shaped to a flat plate with a thickness of 0.3 mm using the MNSed CoCrMo die. The medical surgery tools can be formed by the combination of upsetting and near-net forging with the use of an MNSed CoCrMo die. As reported in [32], these near-net forged AISI316 tools are expected to work as surgery steel instruments with high mechanical reliability and strength.

When using normal stainless steel as a die for molding stamping of oxide glasses, their grain boundaries are also imprinted to the glass work without the amorphous coating such as NiP or NiWP [33]. The nanostructured top and buffer layers of the MNSed CoCrMo die were machined and surface-finished to have low surface roughness in adaptive to the mold-stamping of oxide glass works even with high glass transition temperature [34,35]. Recently, oxide glass work materials with higher glass transition temperatures than 1073 K are required for functional optical elements [36]. The conventional AISI360 dies with sufficiently low surface roughness and high surface finish, making it easy to make dimensional distortion during mold stamping at elevated temperatures. MNSed CoCrMo dies with well-defined surface quality provide a solution to this mold stamping of oxide glass works at elevated holding temperature.

As partially stated in [37], the self-nanostructuring of multi-host-metal alloys, such as AISI316 and high-entropy alloys [38], accompanies the nano-scaled phase separation among multi-metal components. Further fine microstructural analysis is needed to describe the possibility of this phase separation in the CoCrMo and other high-entropy alloys by MNS and to explain the effect of this phase separation on the machinability in finishing to build up the dies and molds.

5. Conclusions

The CoCrMo superalloy is modified by massive nitrogen supersaturation at 723 K by 60 Pa for 21.6 ks to have a multi-layered microstructure, where the nanostructured MNS layer, the buffer layer, and the textured layer are formed into the original CoCrMo die. This unique structure induces the graded hardness profile into a homogeneous CoCrMo alloy. The top layer with higher hardness than 1300 HV_{1N} and a thick hardness grading system from this top layer to the depth across the buffer layer work as a low-wearing die for upsetting the fine-grained AISI316 bars with high flow stress. BOD testing and upsetting experiments demonstrate the engineering integrity of MNSed CoCrMo dies enough to be used for near-net forging of fine-grained AISI316 feedstock to yield reliable surgical steel instruments.

Since the original CoCrMo die has sufficient thermal resistance, this MNSed CoCrMo is also useful as a mold to imprint its highly finished surface onto the oxide glass work materials with high glass transition temperature during the hot stamping process. The nanostructured surface of the MNSed CoCrMo die proves the highly finished surface of the oxide glass lens and optical elements.

Author Contributions: Conceptualization, T.A.; methodology, T.A. and T.F.; validation, T.A., T.F. and T.S.; investigation, T.A., T.F. and T.S.; resources, T.F.; data curation, T.A. and T.F.; writing—original draft preparation, T.A.; writing—review and editing, T.S.; supervision, T.F. All authors have read and agreed to the published version of the manuscript.

Conflicts of Interest: Author Tatsuya Fukuda was employed by the company Tokai Engineering Service, Co., Ltd. The remaining authors declare that the research was conducted in the absence of any commercial or financial relationships that could be construed as a potential conflict of interest.

References

1. Aizawa, T.; Shiratori, T.; Komatsu, T. Integrated manufacturing of fine-grained stainless steels for industries and medicals. In *High Entropy Alloys*; IntechOpen: London, UK, 2019; Chapter 4; pp. 1–22.
2. Komatsu, T. *Private Communication on the Workability of Complex-Shaped High Strength AISI316 Wires and Bars*; Suwa, Japan, 2024.
3. Cui, C.; Ping, D.; Gu, Y.; Harada, H. A new Co-base superalloy strengthened by γ′ phase. *Mater. Trans.* **2006**, *47*, 2099–2102. [CrossRef]
4. Bettin, E.; Leygraf, C.; Pan, J. Nature of current increase for a CoCrMo alloy: Transpassive dissolution vs. water oxidation. *Int. J. Electrochem. Sci.* **2013**, *8*, 11791–11804. [CrossRef]
5. Cheng, H.; Xu, M.; Zhang, H.; Wu, W.; Zheng, M.; Li, X. Cyclic fatigue properties of cobalt-chromium alloy clasps for partial removable dental protheses. *J. Prosthet. Dent.* **2010**, *104*, 389–396. [CrossRef]
6. Funazuka, T.; Horiuchi, S.; Dohda, K.; Shiratori, T. Effect of CoCrMo die with nanotexture applied on micro-extrudability of micro backward extrusion of AA6063. In Proceedings of the 6th World Congress on Micro and Nano Manufacturing WCMNM2023, Evanston, IL, USA, 9 September 2023; pp. 1–4.
7. Aizawa, T.; Fukuda, T. Dry cold forging of AISI316 bars by massively nitrogen supersaturated CoCrMo. In Proceedings of the 10th ICTMP Conference, Alcoy, Spain, 24 June 2024; in press.
8. Lee, S.; Nomura, N.; Chiba, A. Significant improvement in mechanical properties of biomedical Co-Cr-Mo alloys with combination of N addition and Cr-enrichment. *Mater. Trans.* **2008**, *2*, 260–264. [CrossRef]
9. Wang, Q.; Zhang, L.; Shen, H. Microstructure analysis of plasma nitrided cast/forged CoCrMo alloys. *Surf. Coat. Technol.* **2010**, *205*, 2654–2660. [CrossRef]
10. Dong, H. S-phase surface engineering of Fe-Cr, Co-Cr and Ni-Cr alloys. *Int. Mater. Rev.* **2011**, *55*, 65–98. [CrossRef]
11. Shukla, K.; Sugumaran, A.A.; Khan, I.; Ehiasarian, A.P.; Hovsepian, P.E. Low pressure plasma nitrided CoCrMo alloy utilizing HIPIMS discharge for biomedical applications. *J. Mech. Behav. Biomed. Mater.* **2020**, *111*, 104110. [CrossRef]
12. Zhang, L.; Liu, W. Precision glass molding: Toward an optimal fabrication of optical lenses. *Front. Mech. Eng.* **2017**, *12*, 3–17. [CrossRef]

13. Smolik, J. Hard Protective Layers on Forging Dies—Development and Applications. *Coating* **2021**, *11*, 376. [CrossRef]

14. Zhai, W.; Zhou, W. Grain refinement and strengthening of 316L stainless steel through addition of TiC nanoparticles and selective laser melting. *Mater. Sci. Eng. A* **2022**, *832*, 142460. [CrossRef]

15. Shang, Z.; Niu, H.; Wei, X.; Song, D.; Zou, J.; Liu, G.; Liang, S.; Nie, L.; Gong, X. Microstructure and tensile behavior of nickel-based single crystal superalloys with different Re contents. *J. Mater. Res. Technol.* **2022**, *18*, 2458–2469. [CrossRef]

16. Yakubov, V.; Kruzic, J.J.; Li, X. Heat-resistant intermetallic compounds and ceramic dispersion alloys for additive manufacturing: A Review. *Adv. Eng. Mater.* **2022**, *24*, 2200159. [CrossRef]

17. Aizawa, T.; Funazuka, T.; Shiratori, T.; Suzuki, Y. Massive nitrogen supersaturation to CoCrMo alloys for surface microstructure control. *Acad. Mater. Sci.* **2023**, *1*, 1–9. [CrossRef]

18. Aizawa, T.; Funazuka, T.; Shiratori, T.; Suzuki, Y. Massive nitrogen supersaturation into CoCrMo alloys for improvement of tribological performance. *Mater. Res. Proc.* **2024**, *41*, 1248–1258.

19. Aizawa, T.; Rsadi, I.; Yunata, E.E. High density RF-DC plasma nitriding under optimized conditions by plasma-diagnosis. *Appl. Sci.* **2020**, *12*, 3706. [CrossRef]

20. Sharma, M.K.; Saikia, B.K.; Bujarbarua, S. Optical emission spectroscopy of DC pulsed plasmas used for steel nitriding. *Surf. Coat. Technol.* **2008**, *203*, 229–233. [CrossRef]

21. Torizuka, S.; Muramatsu, E.; Murty, S.V.S.N.; Nagai, K. Microstructure evolution and strength-reduction in area balance of ultrafine-grained steels processed by warm caliber rolling. *Scr. Mater.* **2006**, *55*, 751–754. [CrossRef]

22. Manova, D.; Lotnyk, A.; Mändl, S.; HNeumann, H.; Rauschenbach, B. CrN precipitation and elemental segregation during the decay of expanded austenite. *Mater. Res. Express* **2016**, *3*, 066502. [CrossRef]

23. Caleb EAndrews, C.E.; Maria Strantza Calta, N.P.; Matthews, M.J.; Taheri, M.L. A denoising autoencoder for improved Kikuchi pattern quality and indexing in electron backscatter diffraction. *Ultramicroscopy* **2023**, *253*, 113810. [CrossRef]

24. Dohda, K.; Yamamoto, M.; Hu, C.; Dubar, L.; Ehmann, K.F. Galling phenomena in metal forming. *Friction* **2021**, *9*, 665–685. [CrossRef]

25. Weidner, A. Plastic deformation and strain localizations. In *Deformation Processes in TRIP/TWIP Steels*; Springer: Berlin/Heidelberg, Germany, 2020; pp. 7–45.

26. Hong, J.-J.; Yeh, W.-C. Application of response surface methodology to establish friction model of upset forging. *Adv. Mech. Eng.* **2018**, *10*, 1687814018766744. [CrossRef]

27. Domain, C.; Becqart, C.S.; Foct, J. Ab initio study of foreign interstitial atom (C, N) interactions with intrinsic point defects in a-Fe. *Phys. Rev. B* **2004**, *69*, 144122. [CrossRef]

28. Borgioli, F.; Galvanetto, E.; Bacco, T. Low temperature nitriding of AISI300 and 200 series austenitic stainless steels. *Vacuum* **2018**, *1016*, 51–60.

29. Dohda, K.; Boher, C.; Rezai-Aria, F.; Mahayotsanun, N. Tribology in metal forming at elevated temperatures. *Friction* **2015**, *3*, 1–27. [CrossRef]

30. Nunthavarawong, P.; Rangappa, S.M.; Siengchin, S.; Dohda, K. *Diamond-Like Carbon Coatings-Technologies and Applications*; CRC-Press: Boca Raton, FL, USA, 2023.

31. Fei Sun, F.; Liu, X.-L.; Luo, S.-Q.; Xiang, D.-D.; Ba, D.-C.; Lin, Z.; Song, G.-Q. Duplex treatment of arc plasma nitriding and PVDTiN coating applied to dental implant screws. *Suf. Coat. Technol.* **2022**, *439*, 128449. [CrossRef]

32. Knowledge Base by ANIMA-Lab. Available online: https://animalab.eu/knowledge-base/which-alloy-is-best-for-my-surgical-instruments (accessed on 1 October 2024).

33. Lelevic, A.; Walsh, F.C. Electrodeposition of Ni-P alloy coatings: A review. *Surf. Coat. Technol.* **2019**, *369*, 198–220. [CrossRef]

34. Saito, H.; Tei, K.; Shamoto, E.; Hara, T. Fine machining of nitrided steels. *Proc. JSPE* **2017**, *2017*, 873–874.

35. Aizawa, T.; Fukuda, T. Microstructure and micro-machinability of plasma nitrided AISI420 martensitic stainless steels at 673 K. In *Chapter 1 in Top 5 Contributions in Materials Sciences*, 6th ed.; AVID Science: Hyderabad, India, 2019; pp. 2–23.

36. Yongchang Guo, Y.; Li, J.; Ying Zhang, Y.; Feng, L.; Sun, H. High-entropy R_2O_3-Y_2O_3-TiO_2-ZrO_2-Al_2O_3 glasses with ultrahigh hardness, Young's modulus, and indentation fracture toughness. *iScience* **2021**, *24*, 102735.

37. Aizawa, T. Micro-/meso-structure control of multi-hostmetal alloys by massive nitrogen supersaturation. *J. Mater.* **2024**, *17*, 1294. [CrossRef]

38. George, E.P.; Raabe, D. High entropy alloys. *Nat. Rev. Mater.* **2019**, *4*, 515–534. [CrossRef]